Research Article

Nano Research
2022, 15(10): 8962–8971

ISSN 1998-0124 CN 11-5974/O4
https://doi.org/10.1007/s12274-022-4532-y

Tuning Li-excess to optimize Ni/Li exchange and improve stability of structure in $LiNi_{0.8}Co_{0.1}Mn_{0.1}O_2$ cathode material for lithium-ion batteries

Fangya Guo[§], Yongfan Xie[§], and Youxiang Zhang (✉)

College of Chemistry and Molecular Sciences, Wuhan University, Wuhan 430072, China
[§] *Fangya Guo and Yongfan Xie contributed equally to this work.*

© Tsinghua University Press 2022

Received: 30 March 2022 / **Revised:** 6 May 2022 / **Accepted:** 14 May 2022

ABSTRACT

Ni/Li exchange is a detrimental effect on electrochemical performances for high-Ni cathode materials ($LiNi_xCo_yMn_zO_2$, $x \geq 0.6$). Adjusting Li-excess degree has been proved to be an effective way to optimize Ni/Li exchange in the materials. However, until now, how the Ni/Li exchange and thus the structural properties is affected by the Li-excess has not been understood and clearly elucidated in the literature. Herein, a feasible strategy is utilized to optimize Ni/Li exchange and the amount of anti-Li^+ in $LiNi_{0.8}Co_{0.1}Mn_{0.1}O_2$ by mixing $Ni_{0.8}Co_{0.1}Mn_{0.1}(OH)_2$ precursor with different amounts of lithium sources during lithiation. It was found that morphology and phase stability of the material can be tuned with moderate excessive lithium. With 10% Li-excess, $LiNi_{0.8}Co_{0.1}Mn_{0.1}O_2$ exhibits an initial discharge capacity of 211.5 $mAh \cdot g^{-1}$ at 0.1 C and maintains 93.3% of its initial capacity after 100 cycles at 1 C. Different technologies were used to characterize the materials and it shows that the formation of broader Li slab space, decreased anti-Ni^{2+} in Li layer, and gradient distribution of Ni^{3+} in the surface is contributed to moderate Li-excess in the materials. Broader Li slab space facilitates diffusion of Li^+, decreased antisite-Ni^{2+} and gradient distribution of Ni^{3+} in materials surfaces optimizes the Ni/Li exchange. Based on these results, we thus believe that it is the moderate Li-excess in material that optimized the electrochemical performance of high-Ni cathode materials.

KEYWORDS

Ni-rich cathodes, Ni/Li exchange, Li-excess, structural stability, cycling stability

1 Introduction

To realize the high energy density for lithium-ion batteries is one of the foremost academic and engineering challenges in the 21st century [1–3]. Layered lithium transition metal oxides ($LiMO_2$) with various compositions have been extensively applied in electric vehicles and plug-in hybrid electric vehicles. Particularly, Ni-rich Li $(Ni_xCo_yMn_z)O_2$ ($x + y + z = 1$ and $x \geq 60\%$) cathode materials have received great attention due to their higher density and lower price compared with traditional nickel cobalt manganese oxide (NCM) materials [4–6]. However, Ni/Li exchange always happens between Li layer and transition metal layer during the high temperature synthesis and electrochemical cycling owing to the similar ionic radius for Li^+ and Ni^{2+} (Ni^{2+}: 0.69 Å, Li^+: 0.76 Å) [7–9].

In fact, Ni/Li exchange is not only one type of intrinsic structural imperfections for layered transition metal oxides, which influences the electrochemical performance of materials, but also tightly associated with irreversible phase transition and the formation of microcracks for secondary particle agglomerates [10–12]. To be more specific: (1) The Ni^{2+} in Li layers decreases the Li-O layer spacing, which impedes the migration of Li-ions [13, 14]. (2) The antisite Ni^{2+} in Li layer may gradually migrate to surface of the materials during cycling, which is benefit from the low migration barrier for the antisite-Ni^{2+} and results in the depletion of Ni and phase transition. Thus, it leads to the fade of capacity during cycling [15–17]. (3) Ni/Li exchange aggravates the anisotropic stress for secondary particles, which mismatches grains and brings microcracks. The electrolyte can easily penetrate the internal of materials and lead to the degradation at primary particles [18–20].

Hence, it's important to tune the degree of Ni/Li exchange to optimize the electrochemical properties for Ni-rich materials. Tremendous efforts have been made to solve this problem [21–25]. For the AMO_2 composition, if the cation sizes are different for A^+ and M^{3+}, it will be favor to form α-$NaFeO_2$ structure. Thus, the $LiNi_{0.5}Mn_{0.5}O_2$ with low Ni/Li disordering was synthesized by ion exchange from $NaNi_{0.5}Mn_{0.5}O_2$ [26]. Wang et al [27]. also provided that the Ni/Li exchange could be reduced by the way of post-synthesis annealing at an optimum temperature 400 °C for $LiNi_{0.8}Co_{0.1}Mn_{0.1}O_2$. Nevertheless, Ni/Li exchange will be return to a higher level if the annealing temperature exceeds 500 °C due to the loss of oxygen atoms. Precursor preoxidation was also an effective method to modulate Ni/Li exchange for Ni-rich cathode materials. The NiOOH phase emerged after the $Ni_{0.8}Co_{0.1}Mn_{0.1}(OH)_2$ was preoxidized by $Na_2S_2O_8$ for 60 min, which indicated a fraction of Ni^{2+} transformed to Ni^{3+} [28]. The peroxidation of the hydroxide precursor diminished Ni/Li exchange for the cathode materials and provided an innovative

Address correspondence to yxzhang04@whu.edu.cn

method to solve the cation mixing by decreasing the contents of Ni^{2+}.

Although the elaborate efforts have been made to optimize the Ni/Li exchange, most previous studies were too complicated for practical production. Reducing the ratios of Ni^{2+} by low valence states of metals to substitute of TM cations was considered an effective way to optimize Ni/Li exchange because the Ni^{2+} is easier to be oxidized compared with oxidation of Mn^{4+} and Co^{3+} [29, 30]. Thus, Zhang et al. [31] provided that increasing the ratio of x in the $Li_{1+x}(NMC)_{1-x}O_2$ to decrease the amounts of Ni^{2+} by substitution of Li^+. However, the increase of x may lead to the loss of specific capacity in the $Li_{1+x}(NMC)_{1-x}O_2$ systems. Moreover, the optimum ratio of Li^+-antisite in the TM layer has not been invested [32]. Therefore, in our work, the Ni-rich cathode materials with different ratios of Li^+-antisite in the TM layer were synthesized by mixing $Ni_{0.8}Co_{0.1}Mn_{0.1}(OH)_2$ precursor with different degrees of Li-excess (with respect to TMs). The excessive lithium not only plays a role of molten salt to promote the merge of nano-primary particles, but also substitutes the Ni^{2+} in the TM layer to optimize Ni/Li exchange without sacrificing the specific capacity. X-ray powder diffraction (XRD), scanning electron microscopy (SEM), and scan transmission electron microscope and electron energy loss spectroscopy (STEM-EELS) were performed in order to investigate the Ni/Li exchange ratio, the lattice parameters, and microstructural changes of samples. The $LiNi_{0.8}Co_{0.1}Mn_{0.1}O_2$ (Li:TM = 1.1) with a proper ratio (5.97%) of Li^+-antisite in TM layer exhibits the optimum electrochemical performance compared with other materials. The result can be attributed to the larger slab of LiO_2 and optimized Ni/Li cation mixing, which promotes the diffusion of Li^+ and maintain the structure stability.

2 Experiment

2.1 Material synthesis

$Ni_{0.8}Co_{0.1}Mn_{0.1}(OH)_2$ precursor was prepared by a typical co-precipitation method, using a continuously stirred tank reactor with N_2 atmosphere. Appropriate ratio of $NiSO_4{\cdot}6H_2O$, $CoSO_4{\cdot}7H_2O$, and $MnSO_4{\cdot}H_2O$ were dissolved in distilled water with molar ratios of Ni/Co/Mn = 8/1/1 to form a 2 M solution. Firstly, 1 L distilled water was added to the reactor (capacity 5 L). Then the transition metal sulfates were added into the continuous stirring tank reactor (CSTR) using digital peristaltic pump. Meanwhile, the 6 M NaOH and 2 M $NH_3{\cdot}H_2O$ were separately added into reactor. The pH value (pH = 11.4), stirring speed (850 rpm), and temperature (50 °C) were controlled by digital peristaltic pump during the precipitation process. After aging reaction, the precipitate was washed with water to decrease the pH value to 7. The precipitate was dried in a vacuum drying oven at 80 °C for 12 h. $Ni_{0.8}Co_{0.1}Mn_{0.1}(OH)_2$ precursor was mixed with different degrees of excessive $LiOH{\cdot}H_2O$, ground sufficiently, preliminarily calcined at 500 °C for 6 h and followed calcined at 750 °C for 12 h under an O_2 atmosphere to synthesize cathode materials. Herein, the obtained cathode materials by setting ratio between $LiOH{\cdot}H_2O$ and $Ni_{0.8}Co_{0.1}Mn_{0.1}(OH)_2$ to 1:1, 1.05:1, 1.1:1, 1.2:1, and 1.3:1, and were named as $LiNi_{0.8}Co_{0.1}Mn_{0.1}O_2$ (LNCM)-E00, LNCM-E05, LNCM-E10, LNCM-E20, and LNCM-E30, respectively.

2.2 Structural characterization

The X-ray diffraction profiles of the samples were collected based on Bruker D8 Advance in the range of 10°–80° with Cu Kα radiation. The morphology of the samples was characterized by field emission scanning electron microscopy (FESEM, Zeiss SIGMA). The valence states of TM-ions were determined by ESCALAB 250 X-ray photoelectron spectroscope (XPS, Thermo Fisher Scientific, USA), using C 1s signal (284.8 eV) to calibrated the binding energy of materials. The high-angle annular dark field-STEM (HAADF-STEM) analysis was performed by JEM-ARM200F. The surface area of samples was tested using Brunauer–Emmett–Teller (BET) (ASAP2020). The inductively coupled plasma-atomic absorption spectroscopy (ICP-AAS) was used to analysis the elemental compositions of the materials.

2.3 Electrochemical tests

Electrochemical performance of cathode materials was evaluated by assembling CR2016 coin-type cells. The active materials, acetylene black, and polyvinylidene fluoride were thoroughly mixed with weight ratio of 80:15:5 in the N-methyl pyrrolidinone (NMP) solvent to obtain the slurry. The obtained slurry was spread uniformly on the Al foil and dried in the vacuum oven and then punched into disks as cathode electrodes. The 2016-type coin cells were prepared in an argon-filled glovebox with lithium foils, Celgard 2300 microporous, and 1 M $LiPF_6$ in a 1:1 (v/v) ratio of ethylene carbonate to dimethyl carbonate as anodes, separators, and electrolytes, respectively. Galvanostatic charge–discharge experiments was tested at room temperature with the voltage range of 2.8–4.3 V (vs. Li/Li^+) by the battery test system (Neware, China).

The cyclic voltammogram (CV) measurements were tested on CHI760C electrochemical workstation in the voltage range of 2.8–4.3 V with the scan rate of 0.1 $mV{\cdot}s^{-1}$. Electrochemical impedance spectroscopies (EIS) were also tested with a perturbation amplitude of 5 mV with the frequency of 0.01 to 100 kHz via CHI760C electrochemistry workstation.

3 Results and discussion

3.1 Structure and morphology

XRD patterns of final products with a different degree of excessive lithium are shown in Fig. 1. The diffraction peaks of all the products can be indexed to the α-$NaFeO_2$-type phase with the *R-3m* space group [33]. Impurity phase is not detected except LNCM-E30. Several very small diffraction peaks at 25°–35° can be observed in the enlarged XRD patterns for LNCM-E30, which should be indexed as Li_2CO_3, indicating that all the materials have the orderly layered structured [34]. Rietveld refinement of the XRD data was done to analyses the lattice parameters and evaluate Ni^{2+}/Li^+ cation mixing. The results are displayed in Fig. S1 in the Electronic Supplementary Material (ESM) and Table 1.

In general, Ni^{2+}/Li^+ cation mixing usually happens as an intrinsic structural imperfection due to the similar radius and lower

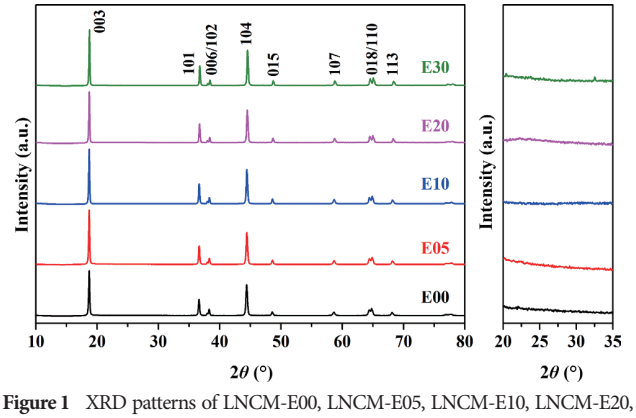

Figure 1 XRD patterns of LNCM-E00, LNCM-E05, LNCM-E10, LNCM-E20, and LNCM-E30.

Table 1 Crystalline structural information about lattice parameters, volume, and Ni/Li disorder ratios of samples after retvield refinement

Samples	LNCM-E00	LNCM-E05	LNCM-E10	LNCM-E20	LNCM-E30
a(Å)	2.8780(9)	2.8762(1)	2.8750(1)	2.8705(4)	2.8686(4)
c(Å)	14.2321(5)	14.2296(4)	14.2244(6)	14.2055(4)	14.2076(8)
v(Å)	102.09(6)	101.95(1)	101.82(3)	101.37(2)	101.25(3)
$d(MO_2)$	2.1423	2.1229	2.1150	2.1062	2.0988
$d(LiO_2)$	2.6017	2.6203	2.6265	2.6289	2.6371
Ni in Li slab (%)	6.34(3)	3.14(1)	2.24(1)	1.67(3)	1.37(8)
Li in Ni slab (%)	1.59(7)	3.78(0)	5.97(1)	7.18(4)	18.38(8)

migration barrier for the Ni^{2+} from TM layers to Li layers [35]. Table 1 shows that the ratio of Ni located in Li layers decreases from 6.34 % in LNCM-E00 to 2.24 % in LNCM- E10, and further to 1.37 % in LNCM-E30. A possible explanation for the phenomenon is that the excessive lithium guarantees more Li^+ saturate Li 3a sites and inhibits Ni^{2+} from entering Li sites. Meanwhile, the ratio of Li^+ located at TM layers increases from 1.57 % in LNCM-E00 to 5.97 % in LNCM-E10, and to 18.38 % in LNCM- E30. Extra Lithium source would saturate 3b sites and decrease the ratio of Ni^{2+}-antisite, resulting in the enlarged Li slab and optimized the Ni/Li cation mixing. At the same time, we argue that, once the Ni^{2+} in TM layers were substituted with part of Li^+, the adjacent Ni^{2+} would be further oxidized to form the Ni^{3+} to maintain the charge balance of materials because the oxidation of Ni^{2+} to Ni^{3+} is easier compared with the oxidation of Co^{3+} and Mn^{4+} to the higher valence [29, 31]. Thus, the contents of Ni^{2+} decreased gradually in the materials surface with increasing the ratio of Li-antisite in the TM layer and formation the Ni^{3+}-rich on the surface of materials.

In order to verify the above scenario, the surface chemistry of the cathode materials was characterized by XPS. Figure 2 displays the Ni $2p_{3/2}$ spectra of LNCM-E00, LNCM-E05, LNCM-E10, LNCM-E20, and LNCM-E30. The most intense Ni $2p_{3/2}$ peak shifted from 854.72 eV for LNCM-E00 to 854.87 eV for LNCM-E10, and to 855.35 eV for LNCM-E30. Meanwhile, the proportions of Ni^{2+}/Ni^{3+} were calculated according to the fitting results, and the relative results were displayed in Tab. S1 in the ESM. It found that the proportion of Ni^{3+} would be increased on the surface of materials with the increasing of ratio of Li^+-antisite and combined with the decreased ratio of Ni^{2+} on the surface of materials. The result demonstrates the scenario that the influence of Li^+-antisite in TM layer on the surface chemistry of materials. It shows that the excessive lithium source promotes the oxidation of Ni^{2+} on the surface of the materials, resulting in optimized the Ni^{2+}/Li^+ cation mixing [36]. Figure S2 in the ESM displays the XPS spectra of Co 2p and Mn 2p for all samples. The oxidation of Co and Mn for all the products are determined to be +3 and +4, respectively, and remain unchanged with the increasing of the excessive lithium.

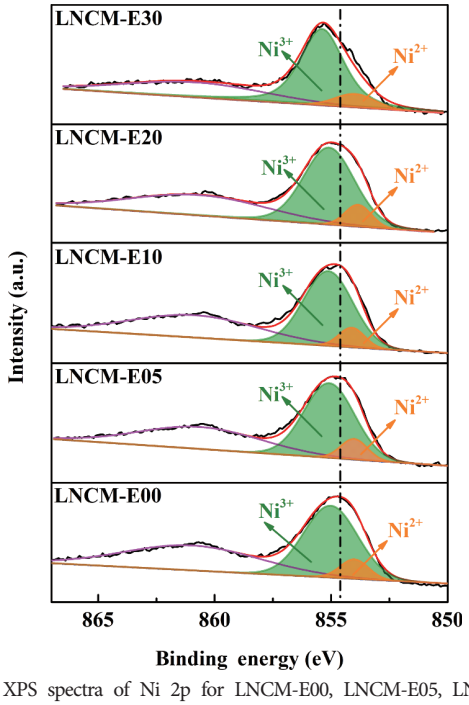

Figure 2 XPS spectra of Ni 2p for LNCM-E00, LNCM-E05, LNCM-E10, LNCM-E20, and LNCM-E30.

Meanwhile, in order to verify the gradient distribution of Ni^{3+} in the material surface due to the Li^+-antisite in the TM layer, the valence of TM for the primary nano-particles at the surface of for LNCM-E00, LNCM-E10, and LNCM-E30 sample was characterized by the STEM-EELS. The chemical and electronic structure of LNCM-E00, LNCM-E10, and LNCM-E30 were acquired by a depth profiling on the surface layer with the depth of ≈ 50 nm (Figs. 3(a), 3(c), and 3(f)) and the EELS profiles of the Ni were displayed in Figs. 3(b), 3(d), and 3(f). Meanwhile, the EELS profiles of the Co and Mn were also displayed in Fig. S3 in the ESM. The ratio of integrated intensities of L3 and L2 is related to the oxidation states of the transition metal. As displayed in Fig. S3 in the ESM, the oxidation states of the Co and Mn not changed for the all materials, which shows the consistent valence state from the core to surface. However, it is different for the surface oxidation of Ni for LNCM-E10 sample by comparing the L3 at Ni-L edge compared to LNCM-E00. In Fig. 3(b), the L3 peak of Ni for LNCM-E10 was obviously changed, which shows the increase of shoulder peak of Ni^{3+} from the core to surface. It demonstrates that the oxidation state of Ni was oxidized from the core to the surface, resulting in the gradient distribution of Ni^{3+} on the surface of materials [37]. The result is consistent with the XPS data. Moreover, the phenomenon of gradient distribution of Ni^{3+} is more evident for LNCM-E30. It is demonstrated that the ratio of Li^+-antisite in the TM layer is the vital factor for the formation of gradient distribution of Ni^{3+} on the material surface. However, once the higher ratio of Ni^{2+} is substituted by Li^+-antisite, the original local Coulombic interaction between Ni-ions, Co-ions, and Mn-ions would be changed. What's worse, the network of superexchange interactions among the TM ions would be also broken. Therefore, the anisotropic stress would be aggravated for the materials and influenced the electrochemical performance [19]. Moreover, the redox reaction $Ni^{2+}/Ni^{3+}/Ni^{4+}$ delivers the specific capacity for $LiNi_{0.8}Co_{0.1}Mn_{0.1}O_2$ electrode. Accordingly, the increasing ratio of Ni^{3+} on the surface of material will lead to the decrease of specific capacity due to sacrifice the oxidation reaction of Ni^{2+}/Ni^{3+}. More importantly, the increasing ratio of Li^+-antisite in the TM layer is due to the excessive lithium source during calcination in the experiment, therefore, it may lead to the more surface contamination (LiOH and Li_2CO_3) and deteriorate

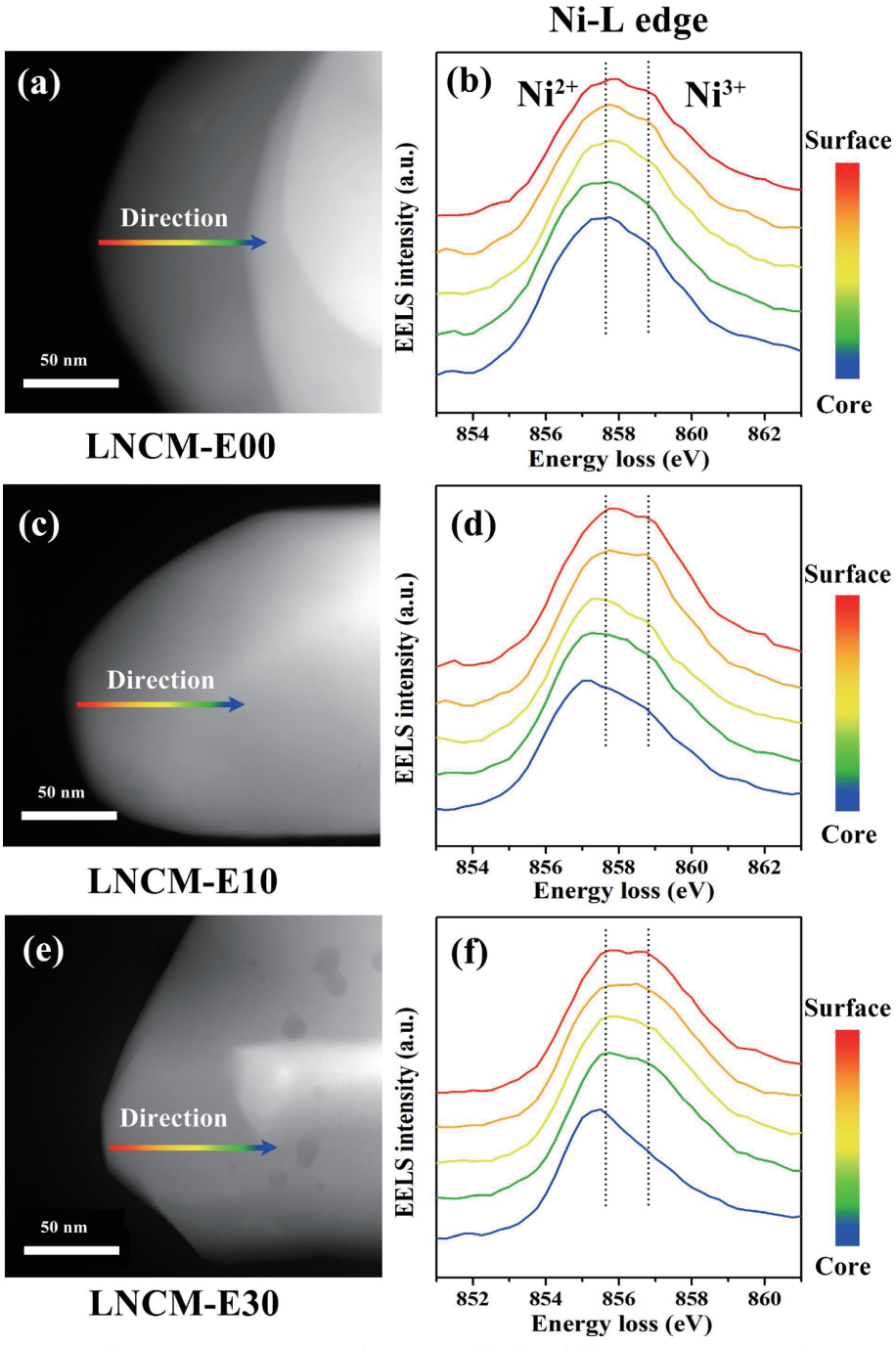

Figure 3 STEM-EELS measurements for LNCM-E00, LNCM-E10, and LNCM-E30. ((a), (c), and (e)) HAADF-STEM image of primary particle for the LNCM-E00, LNCM-E10 and LNCM-E30, and ((b), (d), and (f)) EELS spectra of Ni-L edge recorded on the surface of primary particle of LNCM-E00, LNCM-E10, and LNCM-E30.

the electrochemical performance [38–40]. The chemical compositions of the materials are determined by ICP-AAS and shown in Tab. S2 in the ESM. It is evident that the amounts of Li atom in the materials increase when the Li-excess increase during calcination. It proves that the excessive lithium may lead to the higher contents of residue phase.

Figure S4 in the ESM displays the scanning electron microscope images of the precursor $Ni_{0.8}Co_{0.1}Mn_{0.1}(OH)_2$ power. The precursor shows a secondary particle that assembled by nano-primary particles. Figure 4 displays the SEM images of all materials. It is evident that the final materials retain the spherical secondary morphology, which are aggregated by nano-primary particles. However, it clearly shows that the adjacent primary particles prone to merge with increasing the ratio of excessive source and may lead to decrease the specific surface area of materials, especially for LNCM-E20 and LNCM-E30. From the images of Figs. 4(k), 4(l), 4(n), and 4(o), the primary nano-particles are difficult to distinguish for LNCM-E20 and LNCM-E30. The result of specific surface area of the materials is shown in Fig. S5 in the ESM. It clearly shows that the surface area decreases gradually from LNCM-E00 to LNCM-30. It can be ascribed to that the excessive lithium source plays a role of molten salt, promoting the merge of adjacent nano-primary particles and decreasing the voids in the surface. More important, the relative lower specific surface area can improve the cycling performance by decreasing the contact area between materials and electrolyte and relieve the side reaction [41–43].

3.2 Electrochemical test

To evaluate the effect of excessive lithium on the electrochemical

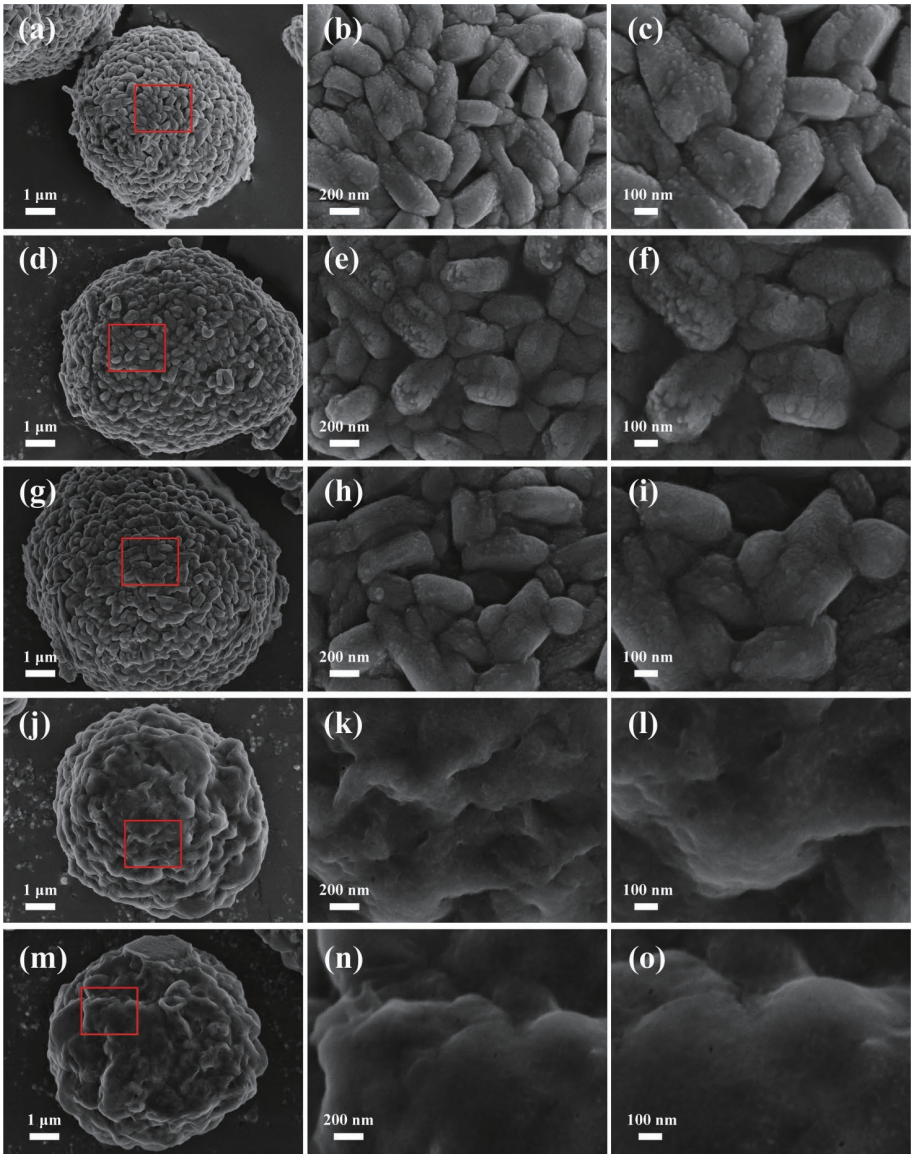

Figure 4 Surface SEM images of materials prepared with different ratio excessive lithium. (a)–(c) LNCM-E00, (d)–(f) LNCM-E05, (g)–(i) LNCM-E10, (j)–(l) LNCM-E20, and (m)–(o) LNCM-E30.

performance of $LiNi_{0.8}Co_{0.1}Mn_{0.1}O_2$, the materials were evaluated by 2016 coin-type half at 25 °C with voltage range from 2.8 to 4.3 V. Electrochemical data is listed in Tab. S3 in the ESM. Figure 5(a) depicts the initial chare–discharge curves of LNCM-E00, LNCM-E05, LNCM-E10, LNCM-E20, and LNCM-E30 at 0.1 C (1 C = 200 $mA{\cdot}g^{-1}$). The discharge specific capacities of these electrodes are 180.0, 205.7, 211.5, 196.2, and 182.6 $mAh{\cdot}g^{-1}$, and the corresponding Coulomb efficiencies are 76.4%, 83.0%, 88.6%, 86.2%, and 82.6%, respectively. The LNCM-E00 shows the lowest discharge capacity and Coulomb efficiency, which is consistent with its highest ratio of Ni^{2+}-antisite. The Ni^{2+}-antisites are oxidized to smaller Ni^{3+} ions and cause the local shrinkage around the Ni-antisite during the charge, resulting in the loss of irreversible capacity and Coulomb efficiency. Meanwhile, the highest discharge specific capacity and Coulomb efficiency for LNCM-E10 are ascribed to the lower ratio of Ni^{2+}-antisite and enlarged Li slab, which promotes the diffusion of Li^+-ions [44]. However, once continuous increase of the ratio of excessive lithium source from LNCM-E10, the discharge specific capacity and corresponding Coulombic efficiency for LNCM-E20 are decreased to 196.2 $mAh{\cdot}g^{-1}$ and 86.2%, respectively, compared to LNCM-E10. The decrease of discharge specific capacity for LNCM-E20 could be attributed to the more Ni^{3+} in the material surface and weaken the oxidation of Ni^{2+}/Ni^{3+}, leading to the less reversible decrease of discharge specific capacity [45]. Specially, though the lowest ratio of Ni^{2+} for LNCM-E30, the broken Coulombic interaction and surface contamination lead to the inferior specific discharge capacity and Coulomb efficiency.

The rate capability was evaluated at various current densities (0.1, 0.5, 1, 2, and 5 C), and then back to 0.1 C and displayed in Fig. 5(b). Apparently, LNCM-E10 shows higher discharge capacities at various current density than other samples. In the 0.1 C rate for the first 5 cycles, LNCM-E10 can deliver around 220 $mAh{\cdot}g^{-1}$ and still can maintain about 140 $mAh{\cdot}g^{-1}$ even at the 5 C rate. Moreover, when the current density backs to 0.1 C, LNCM-E10 retains 96.8% of its initial capacity. The excellent rate performance is attributed to the larger Li slab in LNCM-E10 and lower ratio of Ni^{2+}-antisite, which accelerates the diffusion of Li-ion and maintains the structure stability. Inferior capacities of LNCM-E00 may originate from the highest ratio of Ni^{2+}-antisite, which impedes the diffusion of Li^+ and destroys the structure stability.

Figure 5(c) displays the cycle performance of the electrodes at 1 C for 100 cycles. The LNCM-E00 sample delivers a continues decline of discharge specific capacity, dropping from 157.9 to 132.7 $mAh{\cdot}g^{-1}$ when charge-discharged for 100 cycles, and with

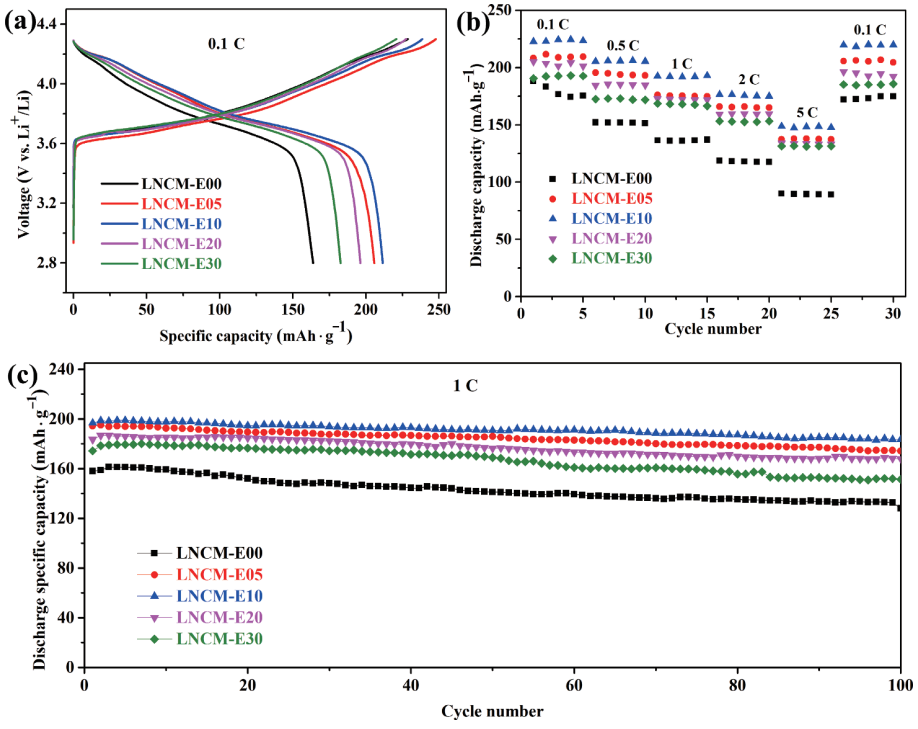

Figure 5 Electrochemical performance of LNCM-E00, LNCM-E05, LNCM-E10, LNCM-E20, and LNCM-E30. (a) Initial charge and discharge at 0.1 C, (b) rate performance, and (c) cycle performance.

capacity retention of 84.0%. The rapid capacity decay for LNCM-E00 is ascribed to the highest ratio of Ni^{2}-antiste, which induces the aggravated anisotropic stress in the bulk structure and destructs the structure stability [46]. However, the introduction of excessive lithium during calcination effectively decreases the ratio of Ni^{2+}-antisite in Li layer and improves remarkable cycling performance. LNCM-E05, LNCM-E10, LNCM-E20, and LNCM-E30 show discharge capacity of 174.3, 183.6, 167.9, and 151.3 mAh·g^{-1} after 100 cycles, with the capacity retentions of 89.6%, 93.3%, 91.5%, and 86.8%. It is obvious that LNCM-E10 exhibits the optimum cycling stability. It demonstrates that a moderate degree of excessive lithium source has a significant effect on adjusting the ratio of Ni^{2+}-antisite in Li layer and suppressing the irreversible phase, resulting in improving the cycling performance. However, though the lowest ratio of Ni^{2+}-antisite for LNCM-E30, the highest ratio of Li^{+}-antisite in the TM layer aggravates the anisotropic press and surface contamination brings inferior cycling performance [20].

The CV profiles of LNCM-E00, LNCM-E05, LNCM-E10, LNCM-E20, and LNCM-E30 from the first to third cycles are shown in Fig. S6 in the ESM. Two pairs of redox peaks are displayed to all CV curves of materials. The oxidation peak with the voltage of 3.5 and 4.0 V is mainly contributed to the redox reaction of $Ni^{2+/4+}$, and another redox peak close 4.2 V represents the redox reaction of Co-ion. Moreover, the difference in the voltage values (ΔE) between anodic peak and cathode peak between 3.5–4.0 V reflects the degree of polarization [47]. For LNCM-E10, the difference is 0.084 V for the initial cycle, which is much less than other four samples, indicating the minute polarization. As the cycling proceeds, the LNCM-E10 shows the minimum values of ΔE than others electrodes. Therefore, it indicates that a proper ratio of excessive lithium source during the calcination can promote the diffusion of Li^{+} and enhance the rate performance.

Figure 6 displays the curves of differential capacity (dQ/dV) vs. the electrode potential, which was obtained from the charge–discharge profiles at 1 C. These curves mainly possess three couples of redox, which relates to structural transition from hexagonal to monoclinic (H1 → M), monoclinic to hexagonal (M → H2), and hexagonal to hexagonal (H2 → H3) [48]. More important, the phase transition from H2 to H3 at ~ 4.2 V causes an abrupt lattice shrinkage along the *c*-direction and then destroys bulk structure, resulting in capacity fading. For the LNCM-E00, as displayed in Figs. 6(a) and 6(b), the anodic peaks continuously shift to higher voltage and the peak intensities gradually decrease with increasing the charge–discharge cycles, especially in the region where the H2 → H3 phase transition. Meanwhile, cathodic peaks shift in the opposite direction and combined with decreasing peak intensity. These results demonstrate that the structural stability has been destroyed with the increasing cycling for LNCM-E00 [49]. After increasing the ratio of excessive lithium, the andic and cathodic peaks at ~ 4.2 V are stable for LNCM-E10. Meanwhile, the position and intensity of peaks are not evidently changed with increasing the cycles, which indicates the phase transition of H2 → H3 has been suppressed. However, the LNCM-E30 has a higher polarization than LNCM-E10 due to the highest ratio of Li^{+}-antisite in the TM layer, which leads to the seriously anisotropic stress for materials due to the changed local Coulombic interaction between TM-ions. These results show that moderate excessive lithium can optimize the Ni/Li exchange and suppress the transition of H2 to H3 and reduce the polarization, resulting enhanced electrochemistry performance especially cycling stability.

To further understand the Li-ion transport behavior with different ratios of excessive lithium, the EIS spectrum was obtained before cycling and after 100 cycles under 1 C at 25 °C.

The EIS spectra were fitted based on the equivalent circuit model in Figs. 7(c) and 7(d). The corresponding fitting data were shown in Table S4 in the ESM. From Fig.7(a) , the Nyquist plots before cycling contain a semicircle in high frequency, which represents the surface charge transfer process (R_{ct}). The sloped line in low-frequency denotes the Warburg impedance. Meanwhile, the small interruption by the semicircle in high frequency relates to the ohmic resistance (R_s) [50, 51]. It is evident that the LNCM-E10 has the minimum R_{ct} and indicates its best cycling stability. Figure 7(b) displays the EIS spectrum of samples after 100 cycles

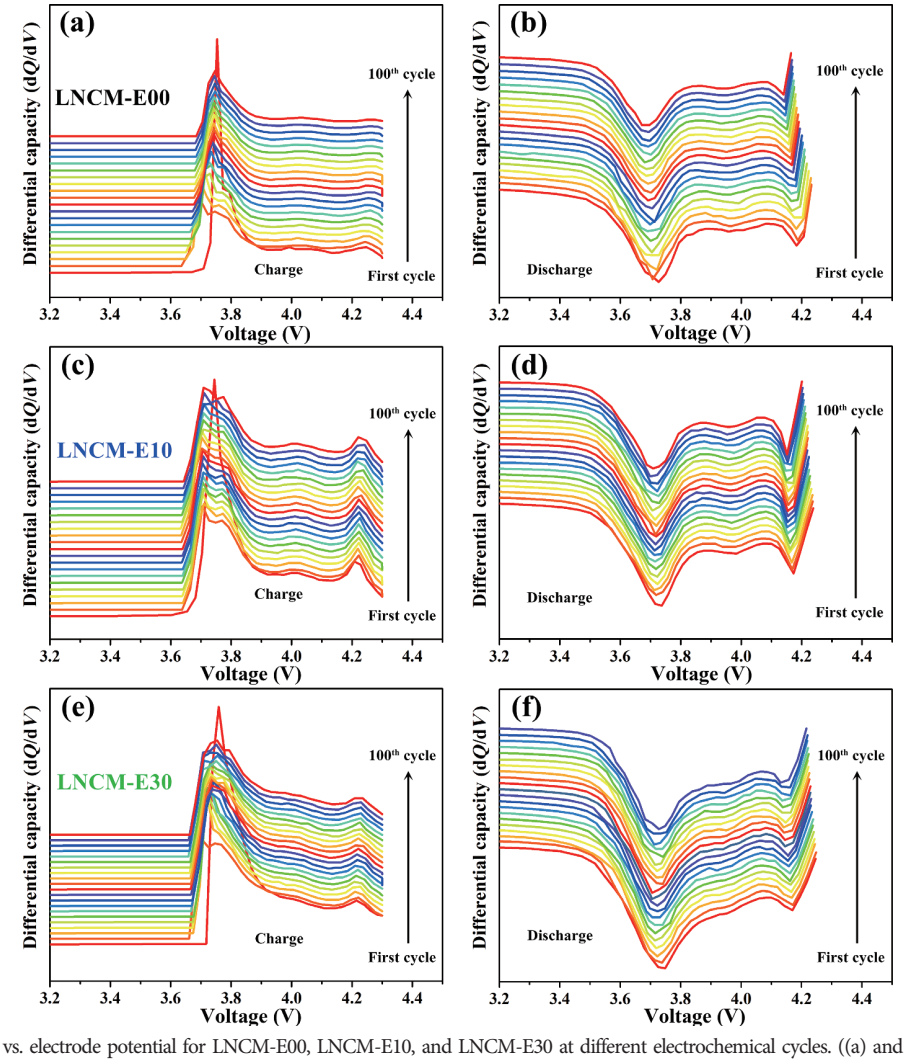

Figure 6 dQ/dV curves vs. electrode potential for LNCM-E00, LNCM-E10, and LNCM-E30 at different electrochemical cycles. ((a) and (b)) LNCM-E00, ((c) and (d)) LNCM-E10, and ((e) and (f)) LNCM-E30.

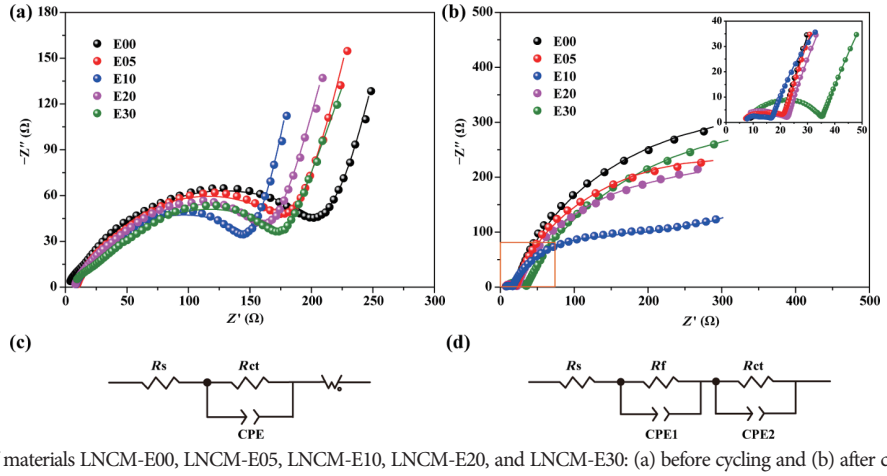

Figure 7 Nyquist plots of materials LNCM-E00, LNCM-E05, LNCM-E10, LNCM-E20, and LNCM-E30: (a) before cycling and (b) after charge–discharge 100 cycles and charged to 4.3 V under 1 C. (c) Equivalent circuit model of materials before cycling and (d) equivalent circuit model of materials after 100 cycles under 1 C.

under 1 C, the plots contain a semicircle in high frequency compared with before cycling denotes the impedance of Li-ion diffusion through the solid electrolyte interphase (SEI) layer (R_{SEI}). After 100 cycles, the R_{ct} for LNCM-E10 switches to 235.1 Ω, while the value for LNCM-E00, LNCM-E05, LNCM-E20, and LNCM-E30 are 745.8, 542.4, 484.8, and 734.3 Ω, respectively. Note that the higher value of R_{ct} for LNCM-E00 after 100 cycles, which can be explained by the highest ratio of Ni^{2+} in Li layer destructs the stability of structure. Moreover, the highest ratio of Li^{+}-antisite brings the anisotropic stress for the LNCM-E30 and destructs the structure stability, resulting in increased values of R_{ct}.

In order to invest the surface condition of cathode materials, the interfacial microstructure of LNCM-E00, LNCM-E10, and LNCM-E30 after 100 cycles under 1 C were performed through high-resolution transmission electron microscopy (HRTEM). The results are depicted in Fig. 8. LNCM-E00 shows the NiO-like rock-salt phase and layered phase at the edge of the surface region according to the Fourier transform images, indicating that the

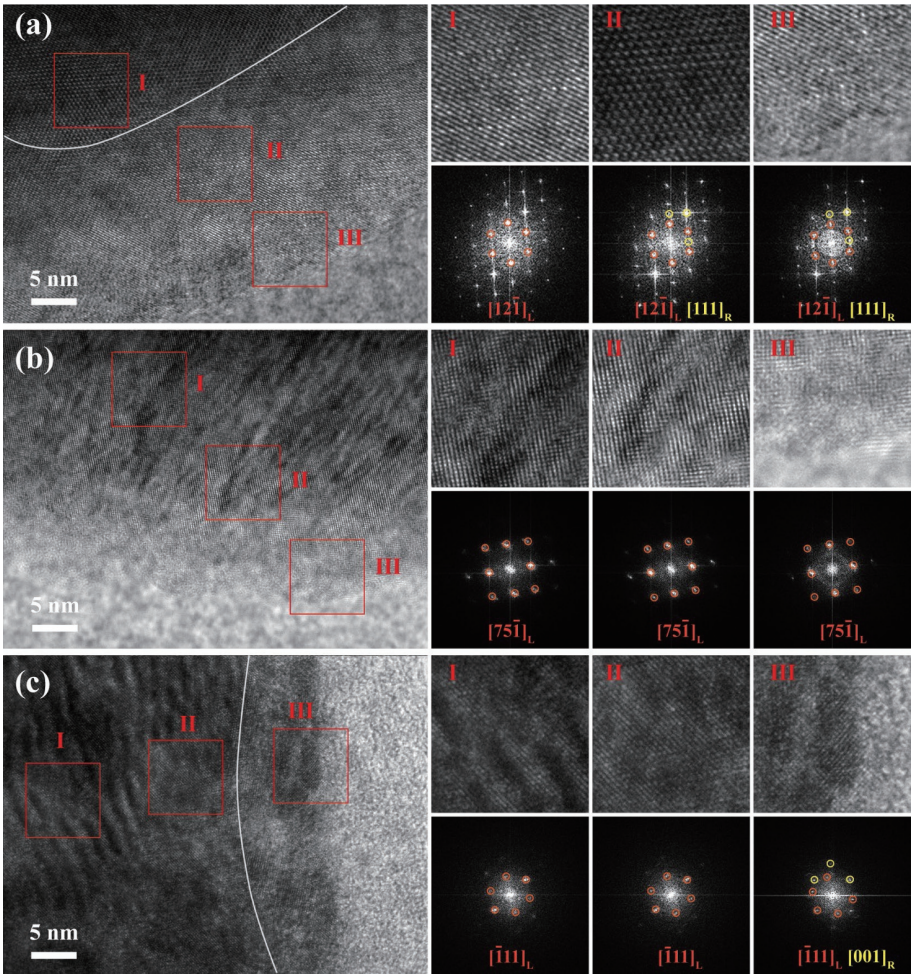

Figure 8 HRTEM images and related FFT patterns of cycled samples of LNCM-E00, LNCM-E10, and LCNM-E30. Marked with red character represents the layered structured and yellow character represents the NiO phase. (a) LNCM-E00, (b) LNCM-E10, and (c) LNCM-E30.

materials underwent [52–54]. It can be explained that the highest ratio of Ni^{2+}-antisite destroys the structure stability and deteriorates the phase transition. The severe Ni/Li exchange could deteriorate the anisotropic stress and lead to the formation of microcracks. Moreover, the electrolyte would penetrate the inner of materials along the microcracks and the side reactions that happen at the interface of electrode/electrolyte would reduce Ni^{4+} to form Ni^{2+}. Especially, the Ni^{2+} is prone to migrate from the TM layers to Li layers due to the similar ionic radius and lower migration barrier, resulting in the structure degradation at the particle edges. For LNCM-E10, the characteristic layered diffraction spot can be seen according to the fast Fourier transform (FFT) images, revealing that the irreversible phase transitions can be suppressed by moderate adjusting the ratio of excessive. However, the higher ratio of Li^+-antisite in the TM layer for LNCM-E30 changes the Coulombic interaction of TM ions and destroys the structure stability. Therefore, the NiO-like rock-salt phase and layered phase emerge on the edge of LNCM-E30. Meanwhile, Fig. S7 in the ESM shows the morphology of LNCM-E00, LNCM-E10, and LNCM-E30 after 100 cycles at 1 C. Many cracks emerge on the surface of LNCM-E00. It is because the highest ratio of Ni^{2+}-antisite aggravates the anisotropic stress between the grains during cycling. The formation of cracks exposes the fresh active materials in the inner of structure, which accelerates the side reaction at the interface between electrode–electrolyte. With the increasing of excessive lithium source, the LNMC-E10 spherical morphology is still maintained. However, the highest ratio of Li^+-antisite for the LNCM-E30 destroys the local Coulombic interaction between TM ions and aggravates the anisotropic stress, resulting in the formation of cracks.

4 Conclusion

In summary, the $LiNi_{0.8}Co_{0.1}Mn_{0.1}O_2$ cathode materials with different ratios of Li^+-antisite in TM layers were synthesized by mixing $Ni_{0.8}Co_{0.1}Mn_{0.1}(OH)_2$ with various excessive lithium source during calcination. LNCM-E10 material with 5.97% Li^+-antisite located at TM layers exhibits excellent electrochemical performance compared with LNCM-E00 (1.97% Li-antisite), LNCM-E05 (3.78% Li-antisite), LNCM-E20 (7.18% Li-antisite), and LNCM-E30 (18.38% Li-antisite). LNCM-E10 shows an initial discharge capacity of 211.5 $mAh{\cdot}g^{-1}$ at 0.1 C with Coulombic efficiencies 88.6% and maintains 93.3% after 100 cycles at 1 C. The excellent electrochemical performance for LNCM-E10 benefits from its optimized structural characters. On one hand, the lower specific surface area can weaken the side reaction between electrode and electrolyte. On the other hand, the decreased ratio of Ni^{2+}-antisite in Li layers and a gradient distribution of Ni^{3+} on the surface together optimize the Ni/Li cation mixing and maintain the structure stability. Less ratio of Li^+-antisite in TM layer means the higher ratio of Ni^{2+}-antisite in the Li layer and brings phase transition for cathode material, resulting in inferior electrochemical performance for LNCM-E00. However, the higher ratio of Li^+-antisite in the TM layer in the material surface may aggravate the anisotropic stress due to the changed of Coulombic interaction and superexchange interactions between TM ions. These findings provide a reasonable explanation for the mechanism that by adding excessive lithium during calcination to optimize the Ni/Li cation mixing and find an optimum ratio of Li^+-

antisite in the TM layer. It will provide a guideline for the industrial production.

Acknowledgements

We thank the National Natural Science Foundation of China (No. 21271145) and the Natural Science Foundation of Hubei Province (No. 2015CFB537) for the financial support for this investigation.

Electronic Supplementary Material: Supplementary material ((rietveld refinement results of LNCM-E00, LNCM-E05, LNCM-E10, LNCM-E20, and LNCM-E30 (Fig. S1); XPS patterns of Co 2p and Mn 2p for LNCM-E00, LNCM-E05, LNCM-E10, LNCM-E20, and LNCM-E30 (Fig. S2); HAADF STEM image of primary particle of LNCM-E00 and EELS spectra of Mn-L edge and Co-L edge recorded on the surface of LNCM-E00, LNCM-E10, and LNCM-E30 (Fig. S3); SEM images of $Ni_{0.8}Co_{0.1}Mn_{0.1}(OH)_2$ precursor (Fig. S4); specific surface area of LNCM-E00,LNCM-E05,LNCM-E10, LNCM-E20, and LNCM-E30 (Fig. S5); CV curves in the first 3 cycles for LNCM-E00, LNCM-E05, LNCM-E10, LNCM-E20, and LNCM-E30 (Fig. S6); SEM images of LNCM-E00, LNCM-E10, and LNCM-E30 after 100 cycles under 1 C (Fig. S7); proportion of Ni^{2+} and Ni^{3+} for LNCM-E00, LNCM-E05, LNCM-E10, LNCM-E20, and LNCM-E30 calculated from XPS data (Table S1); the chemical compositions of the LNCM-E00, LNCM-E05, LNCM-E10, LNCM-E20, and LNCM-E30 measured by ICP-AAS (Table S2); electrochemical data for LNCM-E00, LNCM-E05, LNCM-E10, LNCM-E20, and LNCM-E30 (Table S3); and EIS parameters of LNCM-E00, LNCM-E05, LNCM-E10, LNCM-E20, and LNCM-E30 before and after 100 cycles under 1C (Table S4)) is available in the online version of this article at https://doi.org/10.1007/s12274-022-4532-y.

References

[1] Xiang, F. W.; Cheng, F.; Sun, Y. J.; Yang, X. P.; Lu, W.; Amal, R.; Dai, L. M. Recent advances in flexible batteries: From materials to applications. *Nano Res*., in press, https://doi.org/10.1007/s12274-021-3820-2.

[2] Chen, Y.; Kang, Q.; Jiang, P. K.; Huang, X. Y. Rapid, high-efficient and scalable exfoliation of high-quality boron nitride nanosheets and their application in lithium-sulfur batteries. *Nano Res.* **2021**, *14*, 2424–2431.

[3] Goodenough, J. B.; Park, K. S. The Li-ion rechargeable battery: A perspective. *J. Am. Chem. Soc.* **2013**, *135*, 1167–1176.

[4] Wu, K.; Li, Q.; Dang, R. B.; Deng, X.; Chen, M. M.; Lee, Y. L.; Xiao, X. L.; Hu, Z. B. A novel synthesis strategy to improve cycle stability of $LiNi_{0.8}Co_{0.1}Mn_{0.1}O_2$ at high cut-off voltages through core–shell structuring. *Nano Res.* **2019**, *12*, 2460–2467.

[5] Myung, S. T.; Maglia, F.; Park, K. J.; Yoon, C. S.; Lamp, P.; Kim, S. J.; Sun, Y. K. Nickel-rich layered cathode materials for automotive lithium-ion batteries: Achievements and perspectives. *ACS Energy Lett.* **2017**, *2*, 196–223.

[6] Lai, Y. J.; Li, Z. J.; Zhao, W. X.; Cheng. X. N.; Xu, S.; Yu, X.; Liu, Y. An ultrasound-triggered cation chelation and reassembly route to one-dimensional Ni-rich cathode material enabling fast charging and stable cycling of Li-ion batteries. *Nano Res.* **2020**, *13*, 3347–3357.

[7] Zheng, J. X.; Liu, T. C.; Hu, Z. X.; Wei, Y.; Song, X. H.; Ren, Y.; Wang, W. D.; Rao, M. M.; Lin, Y.; Chen, Z. H. et al. Tuning of thermal stability in layered Li $(Ni_xMn_yCo_z)O_2$. *J. Am. Chem. Soc.* **2016**, *138*, 13326–13334.

[8] Su, Y. F.; Chen, G.; Chen, L.; Lu, Y.; Zhang, Q. Y.; Lv, Z.; Li, C.; Li, L. W.; Liu, N.; Tan, G. Q. et al. High-rate structure-gradient Ni-rich cathode material for lithium-ion batteries. *ACS Appl. Mater. Interfaces* **2019**, *11*, 36697–36704.

[9] Wang, D. W.; Xin, C.; Zhang, M. J.; Bai, J. M.; Zheng, J. X.; Kou, R. H.; Ko, J. Y. P.; Huq, A.; Zhong, G. M.; Sun, C. J. et al. Intrinsic role of cationic substitution in tuning Li/Ni mixing in high-Ni layered oxides. *Chem. Mater.* **2019**, *31*, 2731–2740.

[10] Wang, L. F.; Liu, G. Y.; Ding, X. N.; Zhan, C.; Wang, X. D. Simultaneous coating and doping of a nickel-rich cathode by an oxygen ion conductor for enhanced stability and power of lithium-ion batteries. *ACS Appl. Mater. Interfaces* **2019**, *11*, 33901–33912.

[11] Li, J.; Zhang, M. L.; Zhang, D. Y.; Yan, Y. X.; Li, Z. M. An effective doping strategy to improve the cyclic stability and rate capability of Ni-rich $LiNi_{0.8}Co_{0.1}Mn_{0.1}O_2$ cathode. *Chem. Eng. J.* **2020**, *402*, 126195.

[12] Liu, W.; Oh, P.; Liu, X. E.; Lee, M. J.; Cho, W.; Chae, S.; Kim, Y.; Cho, J. Nickel-rich layered lithium transition-metal oxide for high-energy lithium-ion batteries. *Angew. Chem. , Int. Ed.* **2015**, *54*, 4440–4457.

[13] Zhang, S. S. Problems and their origins of Ni-rich layered oxide cathode materials. *Energy Storage Mater.* **2020**, *24*, 247–254.

[14] Wu, L. P.; Tang, X. C.; Chen, X.; Rong, Z. H.; Dang, W.; Wang, Y.; Li, X.; Huang, L. C.; Zhang, Y. Improvement of electrochemical reversibility of the Ni-rich cathode material by gallium doping. *J. Power Sources* **2020**, *445*, 227337.

[15] Hou, P. Y.; Li, F.; Sun, Y. Y.; Li, H. Q.; Xu, X. J.; Zhai, T. Y. Multishell precursors facilitated synthesis of concentration-gradient nickel-rich cathodes for long-life and high-rate lithium-ion batteries. *ACS Appl. Mater. Interfaces* **2018**, *10*, 24508–24515.

[16] Liu, Y.; Tang, L. B.; Wei, H. X.; Zhang, X. H.; He, Z. J.; Li, Y. J.; Zheng, J. C. Enhancement on structural stability of Ni-rich cathode materials by *in-situ* fabricating dual-modified layer for lithium-ion batteries. *Nano Energy* **2019**, *65*, 104043.

[17] Yan, P. F.; Nie, A. M.; Zheng, J. M.; Zhou, Y. G.; Lu, D. P.; Zhang, X. F.; Xu, R.; Belharouak, I.; Zu, X. T.; Xiao, J. et al. Evolution of lattice structure and chemical composition of the surface reconstruction layer in $Li_{1.2}Ni_{0.2}Mn_{0.6}O_2$ cathode material for lithium-ion batteries. *Nano Lett.* **2015**, *15*, 514–522.

[18] Kim, J. H.; Kim, H.; Kim, W. J.; Kim, Y. C.; Jung, J. Y.; Rhee, D. Y.; Song, J. H.; Cho, W.; Park, M. S. Incorporation of titanium into Ni-rich layered cathode materials for lithium-ion batteries. *ACS Appl. Energy Mater.* **2020**, *3*, 12204–12211.

[19] Yu, H. J.; Qian, Y. M.; Otani, M.; Tang, D. M.; Guo, S. H.; Zhu, Y. B.; Zhou, H. S. Study of the lithium/nickel ions exchange in the layered $LiNi_{0.42}Mn_{0.42}Co_{0.16}O_2$ cathode material for lithium-ion batteries: Experiment and first-principles calculations. *Energy Environ. Sci.* **2014**, *7*, 1068–1078.

[20] Guo, F. Y.; Xie, Y. F.; Zhang, Y. X. Low-temperature strategy to synthesize single-crystal Li $Ni_{0.8}Co_{0.1}Mn_{0.1}O_2$ with enhanced cycling performances as cathode material for lithium-ion batteries. *Nano Res.* **2022**, *15*, 2052–2059.

[21] Zou, Y. H.; Yang, X. F.; Lv, C. X.; Liu, T. C.; Xia, Y. Z.; Shang, L.; Waterhouse, G. I. N.; Yang, D. J.; Zhang, T. R. Multishelled Ni-rich Li $(Ni_xCo_yMn_z)O_2$ hollow fibers with low cation mixing as high-performance cathode materials for Li-Ion batteries. *Adv. Sci.* **2017**, *4*, 1600262.

[22] Zhang, J. D.; Wu, F. Z.; Dai, X. Y.; Mai, Y.; Gu, Y. J. Enhancing the high-voltage cycling performance and rate capability of $LiNi_{0.8}Co_{0.1}Mn_{0.1}O_2$ cathode material by Co-doping with Na and Br. *ACS Sustainable Chem. Eng.* **2021**, *9*, 1741–1753.

[23] Yu, H. F.; Zhu, H. W.; Yang, Z. F.; Liu, M. M.; Jiang, H.; Li, C. Z. Bulk Mg-doping and surface polypyrrole-coating enable high-rate and long-life for Ni-rich layered cathodes. *Chem. Eng. J.* **2021**, *412*, 128625.

[24] Sun, G.; Yin, X. C.; Yang, W.; Song, A. L.; Jia, C. X.; Yang, W.; Du, Q. H.; Ma, Z. P.; Shao, G. J. The effect of cation mixing controlled by thermal treatment duration on the electrochemical stability of lithium transition-metal oxides. *Phys. Chem. Chem. Phys.* **2017**, *19*, 29886–29894.

[25] Cui, J. X.; Ding, X. K.; Luo, D.; Xie, H. X.; Zhang, Z. H.; Zhang, B. Y.; Tan, F. L.; Liu, C. Y.; Lin, Z. Effect of cationic uniformity in precursors on Li/Ni mixing of Ni-rich layered cathodes. *Energy Fuels* **2021**, *35*, 1842–1850.

[26] Kang, K.; Meng, Y. S.; Bréger, J.; Grey, C. P.; Ceder, G. Electrodes with high power and high capacity for rechargeable lithium batteries. *Science* **2006**, *311*, 977–980.

[27] Wang, T.; Ren, K. L.; Xiao, W.; Dong, W. H.; Qiao, H. L.; Duan, A.

R.; Pan, H. Y.; Yang, Y.; Wang, H. L. Tuning the Li/Ni disorder of the NMC811 cathode by thermally driven competition between lattice ordering and structure decomposition. *J. Phys. Chem. C* **2020**, *124*, 5600–5607.

[28] Zhang, C. C.; Liu, M. M.; Pan, G. J.; Liu, S. Y.; Liu, D.; Chen, C. G.; Su, J.; M.; Huang, T.; Yu, A. S. Enhanced electrochemical performance of $LiNi_{0.8}Co_{0.1}Mn_{0.1}O_2$ cathode for lithium-ion batteries by precursor preoxidation. *ACS Appl. Energy Mater.* **2018**, *1*, 4374–4384.

[29] Myung, S. T.; Komaba, S.; Kurihara, K.; Hosoya, K.; Kumagai, N.; Sun, Y. K.; Nakai, I.; Yonemura, M.; Kamiyama, T. Synthesis of Li $[(Ni_{0.5}Mn_{0.5})_{1-x}Li_x]$ O_2 by emulsion drying method and impact of excess Li on structural and electrochemical properties. *Chem. Mater.* **2006**, *18*, 1658–1666.

[30] Zheng, J. X.; Ye, Y. K.; Liu, T. C.; Xiao, Y. G.; Wang, C. M.; Wang, F.; Pan, F. Ni/Li disordering in layered transition metal oxide: Electrochemical impact, origin, and control. *Acc. Chem. Res.* **2019**, *52*, 2201–2209.

[31] Zhang, X. Y.; Jiang, W. J.; Mauger, A.; Qilu; Gendron, F.; Julien, C. M. Minimization of the cation mixing in Li_{1+x} (NMC) $_{1-x}O_2$ as cathode material. *J. Power Sources* **2010**, *195*, 1292–1301.

[32] Yu, Z. L.; Qu, X. Y.; Wan, T.; Dou, A. C.; Zhou, Y.; Peng, X. Q.; Su, M. R.; Liu, Y. J.; Chu, D. W. Synthesis and mechanism of high structural stability of nickel-rich cathode materials by adjusting Li-excess. *ACS Appl. Mater. Interfaces* **2020**, *12*, 40393–40403.

[33] Cheng, Y.; Sun, Y.; Chu, C. T.; Chang, L. M.; Wang, Z. M.; Zhang, D. Y.; Liu, W. Q.; Zhuang, Z. C.; Wang, L. M. Stabilizing effects of atomic Ti doping on high-voltage high-nickel layered oxide cathode for lithium-ion rechargeable batteries. *Nano Res.* **2022**, *15*, 4091–4099.

[34] Peng, S. Y.; Kong, X. B.; Li, J. Y.; Zeng, J.; Zhao, J. B. Alleviating the storage instability of $LiNi_{0.8}Co_{0.1}Mn_{0.1}O_2$ cathode materials by surface modification with poly (acrylic acid). *ACS Sustainable Chem. Eng.* **2021**, *9*, 7466–7478.

[35] Kim, Y.; Kim, D.; Kang, S. Experimental and first-principles thermodynamic study of the formation and effects of vacancies in layered lithium nickel cobalt oxides. *Chem. Mater.* **2011**, *23*, 5388–5397.

[36] Duan, J. G.; Wu, C.; Cao, Y. B.; Huang, D. H.; Du, K.; Peng, Z, D.; Hu, G. R. Enhanced compacting density and cycling performance of Ni-riched electrode via building mono dispersed micron scaled morphology. *J. Alloys Compd.* **2017**, *695*, 91–99.

[37] Kim, J.; Cho, H.; Jeong, H. Y.; Ma, H.; Lee, J.; Hwang, J.; Park, M.; Cho, J. Self-induced concentration gradient in nickel-rich cathodes by sacrificial polymeric bead clusters for high-energy lithium-ion batteries. *Adv. Energy Mater.* **2017**, *7*, 1602559.

[38] Jo, C. H.; Cho, D. H.; Noh, H. J.; Yashiro, H.; Sun, Y. K.; Myung, S. T. An effective method to reduce residual lithium compounds on Ni-rich Li $[Ni_{0.6}Co_{0.2}Mn_{0.2}]$ O_2 active material using a phosphoric acid derived Li_3PO_4 nanolayer. *Nano Res.* **2015**, *5*, 1464–1479.

[39] Robert, R.; Bünzli, C.; Berg, E. J.; Novák, P. Activation mechanism of $LiNi_{0.80}Co_{0.15}Al_{0.05}O_2$: Surface and bulk operando electrochemical, differential electrochemical mass spectrometry, and X-ray diffraction analyses. *Chem. Mater.* **2015**, *27*, 526–536.

[40] Seong, W. M.; Cho, K. H.; Prak, J. W.; Park, H.; Eum, D.; Lee, M. H.; Kim, I. S. S.; Lim, J.; Kang, K. Controlling residual lithium in high-nickel (> 90 %) lithium layered oxides for cathodes in lithium-ion batteries. *Angew. Chem. , Int. Ed.* **2020**, *59*, 18662–18669.

[41] Meng, K.; Wang, Z. X.; Guo, H. J.; Li, X. H.; Wang, D. Improving the cycling performance of $LiNi_{0.8}Co_{0.1}Mn_{0.1}O_2$ by surface coating with Li_2TiO_3. *Electrochim. Acta* **2016**, *211*, 822–831.

[42] Zhang, M. L.; Shen, J. T.; Li, J.; Zhang, D. Y.; Yan, Y. X.; Huang, Y. X.; Li, Z. M. Effect of micron sized particle on the electrochemical properties of nickel-rich $LiNi_{0.8}Co_{0.1}Mn_{0.1}O_2$ cathode materials. *Ceram. Int.* **2020**, *46*, 4643–4651.

[43] Hu, D. Z.; Chen, G.; Tian, J.; Li, N.; Chen, L.; Su, Y. F.; Song, T. L.; Lu, Y.; Cao, D. Y.; Chen, S. et al. Unrevealing the effects of low temperature on cycling life of 21700-type cylindrical Li-ion batteries. *J. Energ. Chem.* **2021**, *60*, 104–110.

[44] Wei, Y.; Zheng, J. X.; Cui, S. H.; Song, X. H.; Su, Y. T.; Deng, W. J.; Wu, Z. Z.; Wang, X. W.; Wang, W. D.; Rao, M. M. et al. Kinetics tuning of Li-ion diffusion in layered Li $(Ni_xMn_yCo_z)O_2$. *J. Am. Chem. Soc.* **2015**, *137*, 8364–8367.

[45] Ma, X. T.; Vanaphuti, P.; Fu, J. Z.; Hou, J. H.; Liu, Y. T.; Zhang, R. H.; Bong, S.; Yao, Z. Y.; Yang, Z. Z.; Wang, Y. A universal etching method for synthesizing high-performance single crystal cathode materials. *Nano Energy* **2021**, *87*, 106194.

[46] Chen, Z.; Wang, J.; Chao, D. L.; Baikie, T.; Bai, L. Y.; Chen, S.; Zhao, Y. L.; Sum, T. C.; Lin, J. Y.; Shen, Z. X. Hierarchical porous $LiNi_{1/3}Co_{1/3}Mn_{1/3}O_2$ nano-/micro spherical cathode material: Minimized cation mixing and improved Li^+ mobility for enhanced electrochemical performance. *Sci. Rep.* **2016**, *6*, 25771.

[47] Meng, K.; Wang, Z. X.; Guo, H. J.; Li, X. H. Enhanced cycling stability of $LiNi_{0.8}Co_{0.1}Mn_{0.1}O_2$ by reducing surface oxygen defects. *Electrochim. Acta* **2017**, *234*, 99–107.

[48] Xu, X.; Huo, H.; Jian, J. Y.; Wang, G. L.; Zhu, H.; Xu, S.; He, X. S.; Yin, G. P.; Du, C. Y.; Sun, X. L. Radially oriented single-crystal primary nanosheets enable ultrahigh rate and cycling properties of $LiNi_{0.8}Co_{0.1}Mn_{0.1}O_2$ cathode material for lithium-ion batteries. *Adv. Energy Mater.* **2019**, *9*, 1803963.

[49] Han, Y. K.; Heng, S.; Wang, Y.; Qu, Q. T.; Zheng, H. H. Anchoring interfacial nickel cations on single-crystal $LiNi_{0.8}Co_{0.1}Mn_{0.1}O_2$ cathode surface via controllable electron transfer. *ACS Energy Lett.* **2020**, *5*, 2421–2433.

[50] Xiao, J. J.; Lin, S. X.; Cai, Z. H.; Muhmood, T.; Hu, X. B. Ultra-high conductive 3D aluminum photonic crystal as sulfur immobilizer for high-performance lithium-sulfur batteries. *Nano Res.* **2021**, *14*, 4776–4782.

[51] Dong, M. X.; Wang, Z. X.; Li, H. K.; Guo, H. J.; Li, X. H.; Shih, K.; Wang, J. X. Metallurgy inspired formation of homogeneous Al_2O_3 coating layer to improve the electrochemical properties of $LiNi_{0.8}Co_{0.1}Mn_{0.1}O_2$ cathode material. *ACS Sustainable Chem. Eng.* **2017**, *5*, 10199–10205.

[52] Li, R.; Bai, C. J.; Liu, H.; Yang, L. W.; Ming, Y.; Xu, C. L.; Wei, Z.; Song, Y.; Wang, G. K.; Liu, Y. X. et al. New insights into the mechanism of enhanced performance of Li $[Ni_{0.8}Co_{0.1}Mn_{0.1}]$ O_2 with a polyacrylic acid-modified binder. *ACS Appl. Mater. Interfaces* **2021**, *13*, 10064–10070.

[53] Qu, X. Y.; Yu, Z. L.; Ruan, D. S.; Dou, A. C.; Su, M. R.; Zhou, Y.; Liu, Y. J.; Chu, D. W. Enhanced electrochemical performance of Ni-rich cathode materials with $Li_{1.3}Al_{0.7}Ti_{1.7}(PO_4)_3$ coating. *ACS Sustainable Chem. Eng.* **2020**, *8*, 5819–5830.

[54] Feng, Z.; Rajagopalan, R.; Sun, D.; Tang, Y. G.; Wang, H. Y. *In-situ* formation of hybrid Li_3PO_4-$AlPO_4$-Al $(PO_3)_3$ coating layer on $LiNi_{0.8}Co_{0.1}Mn_{0.1}O_2$ cathode with enhanced electrochemical properties for lithium-ion battery. *Chem. Eng. J.* **2020**, *382*, 122959.